Chinese Physics B

Excess-iron driven spin glass phase in Fe$_{1+y}$Te$_{1-x}$Se$_x$

To cite this article before publication: Long Tian *et al* 2021 *Chinese Phys. B* in press https://doi.org/10.1088/1674-1056/ac0695

Excess-iron driven spin glass phase in $Fe_{1+y}Te_{1-x}Se_x$

Long Tian(田龙)[1], Panpan Liu(刘盼盼)[1], Tao Hong(洪涛)[2], Tilo Seydel[3], Xingye Lu(鲁兴业)[1]*, Huiqian Luo(罗会仟)[4], Shiliang Li(李世亮)[4], and Pengcheng Dai(戴鹏程)[5]†

[1]Center for Advanced Quantum Studies and Department of Physics, Beijing Normal University, Beijing 100875, China

[2]Neutron Scattering Division, Oak Ridge National Laboratory, Oak Ridge, TN 37831, USA

[3]Institut Max von Laue - Paul Langevin (ILL), 71 Avenue des Martyrs, CS 20156, 38042 Grenoble Cedex 9, France

[4]Beijing National Laboratory for Condensed Matter Physics, Institute of Physics, Chinese Academy of Sciences, Beijing 100190, China

[5]Department of Physics and Astronomy, Rice University, Houston, TX 77005, USA

Abstract

The iron-chalcogenide superconductor $FeTe_{1-x}Se_x$ displays a variety of exotic features distinct from iron pnictides. Although much effort has been devoted to understanding the interplay between magnetism and superconductivity near $x = 0.5$, the existence of a spin glass phase with short-range magnetic order in the doping range ($x \sim 0.1 - 0.3$) has rarely been studied. Here, we use DC/AC magnetization and (quasi)elastic neutron scattering to confirm the spin-glass nature of the short-range magnetic order in a $Fe_{1.07}Te_{0.8}Se_{0.2}$ sample. The AC-frequency dependent spin-freezing temperature T_f generates a frequency sensitivity $\Delta T_f(\omega)/\left[T_f(\omega)\Delta \log_{10}\omega\right] \approx 0.028$ and the description of the critical slowing down with $\tau = \tau_0 \left(T_f/T_{\rm SG} - 1\right)^{-zv}$ gives $T_{\rm SG} \approx 22$ K and $zv \approx 10$, comparable to that of a classical spin-glass system. We have also extended the frequency-dependent T_f to the smaller time scale using energy-resolution-dependent neutron diffraction measurements, in which the T_N of the short-range magnetic order increase systematically with increasing energy resolution. By removing the excess iron through annealing in oxygen, the spin-freezing behavior disappears, and bulk superconductivity is realized. Thus, the excess Fe is the driving force for the formation of the spin-glass phase detrimental to bulk superconductivity.

Keywords: iron chalcogenides, spin glass, neutron scattering

PACS: 74.70.Xa, 75.30.Gw, 78.70.Nx

1. Introduction

Among the family of iron-based superconductors (FeSC), $Fe_{1+y}Te_{1-x}Se_x$ has attracted extensive research interest since its discovery because of its simple structure, availability of air-insensitive large single crystals, and rich electronic and magnetic phases [1–4]. Although much is known about this system, the recent discovery of a topological superconducting state and possible zero-energy Majorana bound states in optimally-doped sample $FeTe_{0.55}Se_{0.45}$ [5–8] have triggered a new wave of intensive investigation.

$Fe_{1+y}Te_{1-x}Se_x$ consists of stacking $FeTe_{1-x}Se_x$ charge-neutral layers along the c axis, and a small amount of excess iron $y \sim 0 - 10\%$ occupying the interstitial positions between the adjacent $FeTe_{1-x}Se_x$ layers [Fig.

*Corresponding author. E-mail:luxy@bnu.edu.cn

†Corresponding author. E-mail:pdai@rice.edu

1(a)]. The antiferromagnetic (AFM) parent compound FeTe orders in a bicollinear magnetic structure [1,2], and superconductivity is established upon substitution of Se for Te to form $FeTe_{1-x}Se_x$ with sufficient large x. The interstitial iron usually exist in the as-grown samples with doping range $x \leq 0.4$ and can heavily affect the intertwined orders of magnetism and superconductivity. With increasing doping, the long-range AFM order gradually decreases and finally vanishes at $x \sim 0.12$ [9–11]. In addition, the filamentary superconductivity emerges at lower doping(Fig. 1(b)). With further doping, superconductivity becomes more robust and reaches its optimal $T_c \approx 15$ K at $x \sim 0.45$.

Although $Fe_{1+y}Te_{1-x}Se_x$ exhibit similar doping evolution of the AFM order and superconductivity as that of iron-pnictides, it is distinct from the latter in several aspects. First, the AFM order with wave vector $Q_T = (0.5, 0.5, L = odd)$ in iron pnictides can be interpreted to be induced by Fermi surface nesting while there is no nesting condition in $Fe_{1+y}Te$, which shows similar Fermi surface topology but different AFM wave vector Q_T=(0.5, 0, L=integer+0.5) [1,2,12,13], suggesting that iron pnictides are dominated by itinerant magnetism (effective moment $\sim 0.9\mu_B$/Fe) while iron chalcogenides by a localized moment ($\sim 2\mu_B$/Fe) [3,11,14–16]. Second, the excess irons located in the interstitial sites (Fe(2) sites in Fig. 1(a)) in $Fe_{1+y}Te_{1-x}Se_x$ can lead to different magnetism by introducing interactions between the local moments of the excess iron and the AFM order lying within the $a-b$ plane [11,17,18]. Third, the AFM spin fluctuations evolve from $\mathbf{Q} = (0.5, 0)$ to (0.5, 0.5) with increasing Se doping in $Fe_{1+y}Te_{1-x}Se_x$, accompanied by the emergence of a neutron spin resonance at (0.5, 0.5). These results suggest that the original bicollinear magnetic order is competing with superconductivity while the emergent collinear spin correlations appear to be strengthened as the superconductivity is optimized [17,19,20].

Although the long-range AFM order in $Fe_{1+y}Te$ is completely suppressed by about 12% of Se doping, there is still short-range magnetic (SRM) order at $\mathbf{Q}_T$=(0.5-δ, 0)(δ=0.02-0.08) in under-doped region persisting to $Fe_{1+y}Te_{0.7}Se_{0.3}$ (y > 0) [2,20–22], where the incommensurability δ can be tuned by the amount of the excess iron. It has been demonstrated that the excess iron is detrimental to superconductivity [17,20] and some earlier investigations suggest that the SRM order in this system exhibits spin-glass behavior accompanied by lattice distortion and competes with superconductivity [22]. As an emergent order intwined with superconductivity, the SRM order is of fundamental importance and deserves a detailed study. We note that such spin-glass/SRM phase have also been observed in similar doping regime of some copper-oxide high-T_c superconductors such as $YBa_2Cu_3O_{6+\delta}$ and $La_{2-x}Sr_xCuO_4$ [23–25], and iron-based superconductors close to the optimal doping [26]. On the other hand, although much efforts have been devoted to establishing the phase diagram of $Fe_{1+y}Te_{1-x}Se_x$ [10,20,22,27], the possible spin-glass state hosting the SRM order in the intermediate doping regime between the long-range AFM order and bulk superconductivity is still under debate. To understand the interplay between the SRM and superconductivity and obtain an accurate phase diagram, it is necessary to clarify the spin-glass phase in this doping regime.

In this work, we have characterized the spin-glass behavior and the SRM order in a $Fe_{1.07}Te_{0.8}Se_{0.2}$ sample using DC/AC magnetization measurements and neutron diffraction method with different energy resolutions varying from $\Delta E \sim 1\mu$eV to 2 meV. The results provide conclusive experimental evidence confirming the spin-glass nature of the SRM order in $Fe_{1.07}Te_{0.8}Se_{0.2}$, suggesting a classical spin-glass ground state of the SRM order. By removing the excess iron in $Fe_{1.07}Te_{0.8}Se_{0.2}$ via annealing in oxygen atmosphere, we find that the spin freezing behavior disappears and bulk superconductivity with a volume fraction larger than 35% can be achieved. These results indicate that the excess Fe in the crystals is the driving force for the spin-glass phase and the SRM order.

2. Materials and experimental details

The $Fe_{1.07}Te_{0.8}Se_{0.2}$ single crystals used in this work were grown by the Bridgman method [4,28]. The doping levels of Se (x) and excess Fe (y), before and after annealing, were measured by inductively-coupled plasma (ICP) analysis. The magnetization measurements were performed on a SQUID-VSM (Vibrating Sample Magnetometer) and a PPMS (Physical Property Measurement System, Quantum Design). Moreover, we carried out neutron scattering measurements on $Fe_{1.07}Te_{0.8}Se_{0.2}$ using the high-resolution neutron backscattering spectrometer IN10 [29] (Experiment number: 4-01-1025) at Institute Laue-Langevin (ILL) and cold neutron triple-axis spectrometer CG-4C [30] at the High-Flux Isotope Reactor (HFIR), Oak Ridge National Laboratory. For the IN10 measurements, thanks to the characteristics of neutron back scattering configuration, we can achieve an energy resolution of 1 μeV with an incident neutron energy of $E_i = 2.08$ meV. For the CG-4C measurements, we used two different incident neutron energies $E_i = 3.2$ meV and 14 meV to get $\Delta E \sim 0.1$ meV and 2 meV, respectively. The DC/AC magnetic susceptibility and neutron diffraction measurements were performed on one piece of single crystal with mass of $\sim$ 0.8-g, while neutron back scattering measurements were carried out on an assembly of co-aligned crystals with a total mass of $\sim$ 6-g. We define the wave vector $\mathbf{Q}$ at (q_x, q_y, q_z) as $(H, K, L) = (q_x a/2\pi, q_y b/2\pi, q_z c/2\pi)$ in reciprocal lattice units (r.l.u.) using the tetragonal unit cell containing two Fe atoms whose a/b axis is along the diagonal direction of the in-plane Fe square lattice, where $a = b = 3.815$ Å and $c = 6.183$ Å. In this notation, the in-plane wave vector for the bicollinear (E-type) AFM order occurs at in-plane wave vector $\mathbf{Q} = (0.5, 0)$ [17].

3. Results and discussion

We first present the basic characterizations of the $Fe_{1.07}Te_{0.8}Se_{0.2}$ sample. Figure 1(c) shows temperature dependence of the in-plane resistivity for undoped $Fe_{1.11}Te$ and doped $Fe_{1.07}Te_{0.8}Se_{0.2}$ samples with excess Fe. The resistivity of the latter exhibits a drastic drop below $T_c = 12$ K but does not reach zero at lower temperature, suggesting filamentary superconductivity. Compared with the parent compound $Fe_{1+y}Te$, which undergoes simultaneous AFM and structural transition manifested as a dramatic decrease in the resistivity at the transition temperature ($T_N = T_S$), $Fe_{1.07}Te_{0.8}Se_{0.2}$ exhibits only a magnetic phase transition associated with the SRM order (Fig. 1(d)) across which the resistivity does not show any feature.

The paramagnetic-to-SRM transition can be clearly seen in the magnetic susceptibility measured on the same sample. In Fig. 1(d), temperature dependent DC magnetic susceptibility χ(T) of $Fe_{1.07}Te_{0.8}Se_{0.2}$ measured with ZFC (zero field cooling) and FCC (field cooled cooling) procedures bifurcate below an irreversibility temperature T_{ir}, revealing a sharp cusp centered at about 22 K in the ZFC curve associated with spin freezing temperature $T_f (< T_{ir})$. Although the bifurcation is an important feature of a spin-glass system, it can also arise from a possible superparamagnetic state. Moreover, some previous studies show that the as-grown $Fe_{1+y}Te_{1-x}Se_x$ sample could contain certain ferromagnetic clusters resulting in a clear ferromagnetic hysteresis in field-dependent magnetization curves. To sort out these two possibilities, we have measured the magnetic-field dependence of the magnetization M(H) at several temperatures across T_f (T=5, 22, 30 K) and way above T_f (T=50, 120, 200 K). As shown in Fig. 1(e), the M(H) curves show linear behavior over the full temperature range, even below $T_f \sim 22$ K, indicating the absence of ferromagnetic clusters and superparamagnetic phase, which usually give 'S'-shape M(H) curves. The linear behavior of M(H) persisting to H=7 T is consistent with the notion that the magnetism is dominated by strong AFM interactions. Concomitantly, the M(H) line at $T = 5$ K, which is below the superconducting transition temperature observed in the resistivity data ($T_c \sim 12$ K) confirms the absence of bulk superconductivity in this sample [31].

To further test the canonical spin-glass behavior, we performed frequency-dependent AC magnetic susceptibility measurements and energy-resolution dependent neutron diffraction on a $Fe_{1.07}Te_{0.8}Se_{0.2}$ crystal (m=0.8

grams). Neutron diffraction rocking curves across the (2, 0, 0) and (0, 0, 1) nuclear Bragg peaks of the sample shows small mosaic (Fig. 1(f)), suggesting high crystalline quality of the sample. AC magnetic susceptibility is an effective tool to characterize the spin-glass behavior, such as the occurrence of the sharp cusp in the AC magnetic susceptibility and its special sensitivity to the frequency of the AC driving field and the magnitude of the external DC field. In Fig. 2(a), we depict temperature dependence of the real part of the AC magnetic susceptibility $\chi'(\omega)$ for $Fe_{1.07}Te_{0.8}Se_{0.2}$ under an AC driving filed H_{AC} = 3 Oe with five different frequencies ranging from 0.1 to 1000 Hz. Each curve shows a peak that obviously shifts towards higher temperature with increasing frequency, which is a typical feature in slow magnetic dynamics of a spin-glass system [32–34]. The temperature corresponding to the peak center in Fig. 2(a) represents the spin glass freezing temperature T_f. The frequency sensitivity of $T_f(\omega)$ can be expressed as $\Delta T_f(\omega)/\left[T_f(\omega)\Delta \log_{10}\omega\right]$, where $\Delta T_f(\omega)$ is the shift of the freezing temperature because of the change in frequency $\Delta \log_{10}\omega$. As for $Fe_{1.07}Te_{0.8}Se_{0.2}$, this value is determined to be 0.028 (Fig. 2(b)), which is comparable to those for several classical spin-glass systems [35], such as the metallic spin-glass CnMn (0.005) [36], insulator spin-glass $Eu_{0.6}Sr_{0.4}S$ (0.05) [36], and II-VI diluted magnetic semiconductors spin-glass $Cd_{0.6}Mn_{0.4}Te$ (0.02) [37].

Through the variation of T_f in a wide frequency range, one can determine a spin glass phase transition based on the divergence of the maximum relaxation time occurring at the spin glass transition temperature T_{SG}, which can be investigated by the conventional critical slowing down [35,38]:

$$\tau = \tau_0 \left(T_f/T_{SG} - 1\right)^{-zv} \tag{1}$$

where τ stands for the measured relaxation time (τ=1/ω), τ_0 represents the flipping time of the magnetic moment and zv is the dynamical critical exponent. The dynamic scaling of the AC magnetic susceptibility is shown in Fig. 2(b), where $\log_{10}\omega$ is plotted as a function of T_f. The best fit to the Eq. (1) yields T_{SG}=21.95 K and zv=10. For a classical spin-glass system, the value of zv usually falls in the range of 4-12 [39,40], namely, the observed scaling phenomenon is consistent with a canonical spin-glass. Figure 2(c) shows temperature dependence of the $\chi'(\omega)$ in two external DC magnetic fields and at $\omega/2\pi$ = 1000 Hz. A sharp cusp is observed at about 24 K without the applied DC field. However, it smears out and shifts toward low temperatures as the applied magnetic field increases, indicating that the spin-glass state is gradually destroyed under a large external magnetic field. Since the magnetic moments begin to freeze below T_f, the system becomes metastable (the valley of the free-energy hypersurface). In a spin-glass state, the (free) energy barrier between metastable states depends on the magnitude of temperature and magnetic field. As the external field increases, the system needs less thermal energy to move from one metastable state to another with lower energy, resulting in the moving down of the T_f [34,41].

Having characterized the spin-glass ground state in $Fe_{1.07}Te_{0.8}Se_{0.2}$ using magnetization, we now turn to the neutron scattering study of the SRM order. In previous neutron scattering work, the SRM order is accompanied by structural glassy behavior [22], manifested as structural distortions across the transition temperature. This is not the case for our sample. As shown in Figs. 3(a) and 3(b), the line shape of the nuclear Bragg peaks (0, 0, 1) and (1, 0, 1) measured at T = 2 K ($T < T_f$) and 60 K ($T > T_f$) show no differences within the instrumental resolution, indicating of no structural transition and lattice distortions in this temperature range. Figures 3(c) and 3(d) display momentum scans along the $[H, 0, 0.5]$ and $[0, 0, L]$ directions at several temperatures measured with E_i = 3.2 meV, in which the scattering at 60 K were subtracted as a background. While the in-plane momentum scans can be well fitted using a single Gaussian, the c-axis magnetic peaks can only be well described with Lorentzian functions. The scans along the $[H, 0, 0.5]$ reveal a broad peak (with a FWHM of ∼0.09 r.l.u.) centered at an incommensurate position (0.45, 0, 0.5), which can be attributed to the SRM order and in line with previous neutron scattering studies. The momentum scans along the $[0.45, 0, L]$ show that the magnetic order is also short-ranged along the c-axis (FWHM∼0.19 r.l.u.). The magnetic correlation length along the a-axis and c-axis calculated from the FWHMs are ∼ 21 Å and ∼ 18 Å, respectively. With

increasing temperature, the magnetic scattering intensity decrease gradually, but remain well defined at $T = 30$ K, which is much higher than the T_f determined from the DC magnetic susceptibility and the fitted $T_{SG} \approx 22$ K. This can be ascribed to the energy-resolution dependence of the freezing temperature measured with neutron scattering.

Temperature dependent order parameters for the SRM order are shown in Fig. 4, measured at $\mathbf{Q} = (0.45, 0, 0.5)$ with different energy resolutions (ΔE) at IN10 and CG-4C spectrometers. While the order parameter measured with neutron back scattering ($\Delta E \sim 1\mu$eV) exhibits a relative sharp intensity change at $T_f = 28.5$ K ($> T_{SG} = 22$ K), the spin-freezing transition shifts to much higher temperatures and becomes rounded as measured by the neutron diffraction with $\Delta E = 0.1$ meV ($T_f = 42 \pm 5$ K) and $\Delta E = 2.0$ meV ($T_f = 48 \pm 5$ K). This energy-resolution dependence of the T_f is a canonical spin-glass behavior, arising from the different time-scale spin dynamics probed with different energy resolution in neutron diffraction measurements. For a typical spin-glass system, the total scattering cross section in neutron diffraction consists of elastic and quasi-elastic scattering (slow dynamics), and temperature-independent nuclear incoherent scattering treated as background. At a high temperature well above $T_f(\omega)$, the total scattering cross section is dominated by incoherent scattering. Upon cooling, slow spin dynamics start to appear. As shown in Eq. (1), the spin dynamics with smaller relaxation time τ can persist to higher temperature. Thus, neutron diffraction measurement with energy resolution ΔE incorporates both elastic scattering and quasielastic scattering with energy transfer $E \leq \Delta E$ ($\tau > h/\Delta E$). With increasing ΔE, slow dynamics with smaller τ (higher E) that can persist to higher temperature will be included in the diffraction signal, leading to a higher-temperature onset of the magnetic order parameter for the SRM order [35,42,43]. The consistency between the $T_f(\Delta E)$ and previous measurements on classical spin-glass systems demonstrates that the SRM order arises from a spin-glass ground state [42,43]. In addition, the AC frequency dependence of the magnetic susceptibility cusps observed in Fig. 2(a) can be construed as approaching the long-relaxation-time limit as in neutron diffraction measurements, where the relaxation time of the spin dynamics probed by $\chi'(\omega)$ equals to $2\pi/\omega$.

Previous studies have shown that, in the intermediate doping regime, the excess iron can be extracted via annealing in air or oxygen environment, by which bulk superconductivity can be achieved for $x \geq 0.1$ [44–46]. In order to check whether the SRM order and spin-freezing in $Fe_{1.07}Te_{0.8}Se_{0.2}$ arise from the effects associated with excess irons, we annealed our sample in oxygen for 7 days [46], which is an effective way to remove excess irons in $Fe_{1+y}Te_{1-x}Se_x$ [44–49]. Figure 5 shows temperature-dependent magnetization curves of an annealed sample measured with ZFC and FCC and H=50 (Fig. 5(a)) and 1000 Oe (Fig. 5(b)). Figure 5(a) displays large diamagnetism below $T_c \sim 12$ K, indicating the emergence of bulk superconductivity in the sample. By contrast, the sharp cusp in the ZFC curve of $Fe_{1.07}Te_{0.8}Se_{0.2}$ vanishes in the annealed sample as shown in Fig. 5(b), suggesting the disappearance of the spin glass phase in the sample. The difference between ZFC and FCC curves at high temperature can be attributed to ferromagnetic impurities formed during the annealing process in oxygen. Previous work shows that the composition and occupancy of a secondary interstitial Fe site in the lattice structure influence the magnetic correlation length [18,45]. These results suggest that the spin glass in $Fe_{1.07}Te_{0.8}Se_{0.2}$ might be attributed to the interaction between the local moments of excess irons and the Fe within the $a - b$ plane.

4. Conclusion

In summary, through exploring the frequency dependence of the spin-freezing temperature (T_f in $\chi'(\omega)$) and the energy-resolution dependent SRM transition temperature using DC/AC magnetization and neutron scattering techniques, we have conclusively identified the spin-glass ground state of $Fe_{1+y}Te_{1-x}Se_x$ in the intermediate doping regime between the long-range AFM order and bulk superconductivity. The dynamic-scaling

analysis of the $\chi'(\omega)$ generates frequency sensitivity of $T_f(\omega)$ and dynamical critical component zv consistent with the parameters in classical spin-glass systems. Through removing the excess iron via annealing, the spin-freezing behavior disappears and bulk superconductivity is realized, suggesting that interactions between excess irons and the Fe in the $FeTe_{1-x}Se_x$ are the driving force of the spin-glass ground state.

Acknowledgment

The work at Beijing Normal University is supported by the National Natural Science Foundation of China (Grant No. 11734002 and 11922402, X.L.). Work at Rice is supported by the US Department of Energy (DOE), Basic Energy Sciences (BES), under Contract No. DE-SC0012311 (P.D.). A portion of this research used resources at the High Flux Isotope Reactor, a DOE Office of Science User Facility operated by the Oak Ridge National Laboratory.

References

[1] Li S L, de la Cruz C, Huang Q, Chen Y, Lynn J W, Hu J P, Huang Y L, Hsu F C, Yeh K W, Wu M K and Dai P C 2009 *Phys. Rev. B* **79** 054503

[2] Bao W, Qiu Y, Huang Q, Green M A, Zajdel P, Fitzsimmons M R, Zhernenkov M, Chang S, Fang M H, Qian B, Vehstedt E K, Yang J H, Pham H M, Spinu L and Mao Z Q 2009 *Phys. Rev. Lett.* **102** 247001

[3] Fang C, Bernevig B A and Hu J P 2009 *EPL* **86** 67005

[4] Wen J, Xu G, Gu G, Tranquada J M and Birgeneau R J 2011 *Rep. Prog. Phys.* **74** 124503

[5] Zhang P, Yaji K, Hashimoto T, Ota Y, Kondo T, Okazaki K, Wang Z J, Wen J S, Gu G D, Ding H and Shin S 2018 *Science* **360** 182-186

[6] Rameau J D, Zaki N, Gu G D and Johnson P D 2019 *Phys. Rev. B* **99** 205117

[7] Wang D F, Kong L Y, Fan P, Chen H, Zhu S Y, Liu W Y, Cao L, Sun Y J, Du S X, Schneeloch J, Zhong R D, Gu G D, Fu L, Ding H and Gao H J 2018 *Science* **362** 333-335

[8] Zhu S Y, Kong L Y, Cao L, Chen H, Papaj M, Du S X, Xing Y Q, Liu W Y, Wang D F, Shen C M, Yang F Z, Schneeloch J, Zhong R D, Gu G D, Fu L, Zhang Y Y, Ding H and Gao H J 2020 *Science* **367** 189-192

[9] Lumsden M D and Christianson A D 2010 *J. Phys.: Condens. Matter* **22** 203203

[10] Khasanov R, Bendele M, Amato A, Babkevich P, Boothroyd A T, Cervellino A, Conder K, Gvasaliya S N, Keller H, Klauss H H, Luetkens H, Pomjakushin V, Pomjakushina E and Roessli B 2009 *Phys. Rev. B* **80** 140511(R)

[11] Martinelli A, Palenzona A, Tropeano M, Ferdeghini C, Putti M, Cimberle M R, Nguyen T D, Affronte M and Ritter C 2010 *Phys. Rev. B* **81** 094115

[12] Xia Y, Qian D, Wray L, Hsieh D, Chen G F, Luo J L, Wang N L and Hasan M Z 2009 *Phys. Rev. Lett.* **103** 037002

[13] Balatsky A V and Parker D 2009 *Physics* **2** 59.

[14] Wilson S D, Yamani Z, Rotundu C R, Freelon B, Bourret-Courchesne E and Birgeneau R J 2009 *Phys. Rev. B* **79** 184519

[15] Mazin I I, Singh D J, Johannes M D and Du M H 2008 *Phys. Rev. Lett.* **101** 057003

[16] Ma F J, Ji W, Hu J P, Lu Z Y and Xiang T 2009 *Phys. Rev. Lett.* **102** 177003

[17] Xu Z J, Wen J S, Xu G Y, Jie Q, Lin Z W, Li Q, Chi S X, Singh D K, Gu G D and Tranquada J M 2010 *Phys. Rev. B* **82** 104525

[18] Bendele M, Babkevich P, Katrych S, Gvasaliya S N, Pomjakushina E, Conder K, Roessli B, Boothroyd A T, Khasanov R and Keller H 2010 *Phys. Rev. B* **82** 212504

[19] Argyriou D N, Hiess A, Akbari A, Eremin I, Korshunov M M, Hu J, Qian B, Mao Z Q, Qiu Y M, Broholm C and Bao W 2010 *Phys. Rev. B* **81** 220503(R)

[20] Liu T J, Hu J, Qian B, Fobes D, Mao Z Q, Bao W, Reehuis M, Kimber S A J, Prokeš K, Matas S, Argyriou D N, Hiess A, Rotaru A, Pham H, Spinu L, Qiu Y, Thampy V, Savici A T, Rodriguez J A and Broholm C 2010 *Nature Materials* **9** 718-720

[21] Wen J S, Xu G Y, Xu Z J, Lin Z W, Li Q, Ratcliff W, Gu G D and Tranquada J M 2009 *Phys. Rev. B* **80** 104506

[22] Katayama N, Ji S, Louca D, Lww S, Fujita M, Sato T J, Wen J S, Xu Z J, Gu G D, Xu G Y, Lin Z W, Enoki M, Chang S, Yamada K and Tranquada J M 2010 *J. Phys. Soc. Japan* **79** 113702

[23] Keimer B, Belk N, Birgeneau R J, Cassanho A, Chen C Y, Greven M and Kastner M A 1992 *Phys. Rev. B* **46** 14034

[24] Koziol Z, Piechota J and Szymczak H 1989 *J. Phys. France* **50** 3123-3131

[25] Sternlieb B J, Luke G M and Uemura Y J 1990 *Phys. Rev. B* **41** 8866

[26] Lu X Y, Tam D W, Zhang C L, Luo H Q, Wang M, Zhang R, Harriger L W, Keller T, Keimer B, Regnault L P, Maier T A and Dai P C 2014 *Phys. Rev. B* **90** 024509
[27] Paulose P L, Yadav C S and Subhedar K M 2010 *EPL* **90** 27011
[28] Chen G F, Chen Z G, Dong J, Hu W Z, Li G, Zhang X D, Zheng P, Luo J L and Wang N L 2009 *Phys. Rev. B* **79** 140509 (R)
[29] Skripov A V, Cook J C, Udovic T J, Gonzalez M A, Hempelmann R and Kozhanov V N 2003 *J. Phys.: Condens. Matter* **15** 3555
[30] Takahashi M, Takeya H, Aczel A A, Hong T, Matsuda M and Kawano-Furukaw H 2018 *Physica B: Condensed Matter* **551** 15
[31] Zhou W, Sun Y, Zhang S, Zhuang J C, Yuan F F, Li X, Shi Z X, Yamada T, Tsuchiya Y and Tamegai T 2014 *J. Phys. Soc. Japan* **83** 064704
[32] Mulder C A M, van Duyneveldt A J, Mydosh J A 1981 *Phys. Rev. B* **23** 1384
[33] Hüser D, Wenger L E, van Duyneveldt A J, Mydosh J A 1983 *Phys. Rev. B* **27** 3100
[34] Li Y, Kan X C, Liu X S, Feng S J, Lv Q R, Ur Rehman K M, Wang W, Liu C C, Wang X H and Xu Y L 2021 *Journal of Alloys and Compounds* **852** 156962
[35] Mydosh J A 2013 *Spin Glasses: An Experimental Introduction* (London: Taylor and Francis) pp.64-72
[36] Tholence J L 1984 *Physics B+C* **126B** 157-164
[37] Mauger A, Ferre J and Nordblad 1988 *Phys. Rev. B* **37** 9022
[38] Hohenberg P C and Halperin B I 1977 *Rev. Mod. Phys.* **49** 435
[39] Gunnarsson K, Sveddh P, Nordblad P and Lundgren L 1988 *Phys. Rev. Lett.* **61** 754
[40] Souletie J and Tholence J L 1985 *Phys. Rev. B* **32** 516
[41] Binder K and Young A P 1986 *Rev. Mod. Phys.* **58** 801
[42] Murani A P 1981 *Journal of Magnetism and Magnetic Materials* **22** pp. 271-281
[43] Murani A P and Heidemann A 1978 *Phys. Rev. Lett.* **41** 1402
[44] Noji T, Suzuki T, Abe H, Adachi T, Kato M and Koike Y 2010 *J. Phys. Soc. Jpn.* **79** 084711
[45] Rodriguez E E, Stock C, Hsieh P Y, Butch N P, Paglione J and Green M A 2011 *Chem. Sci.* **2** 1782
[46] Dong C H, Wang H D, Li Z J, Chen J, Yuan H Q and Fang M H 2011 *Phys. Rev. B* **84** 224506
[47] Koshika Y, Usui T, Adachi S, Watanabe T, Sakano K, Simayi S and Yoshizawa M 2013 *J. Phys. Soc. Jpn.* **82** 023703
[48] Sun Y, Tsuchiya Y, Yamada T, Taen T, Pyon S, Shi Z and Tamegai T 2013 *J. Phys. Soc. Jpn.* **82** 115002
[49] Xu Z J, Schneeloch J A, Yi M, Zhao Y, Matsuda M, Pajerowski D M, Chi S X, Birgeneau R J, Gu G D, Tranquada J M and Xu G Y 2018 *Phys. Rev. B* **97** 214511

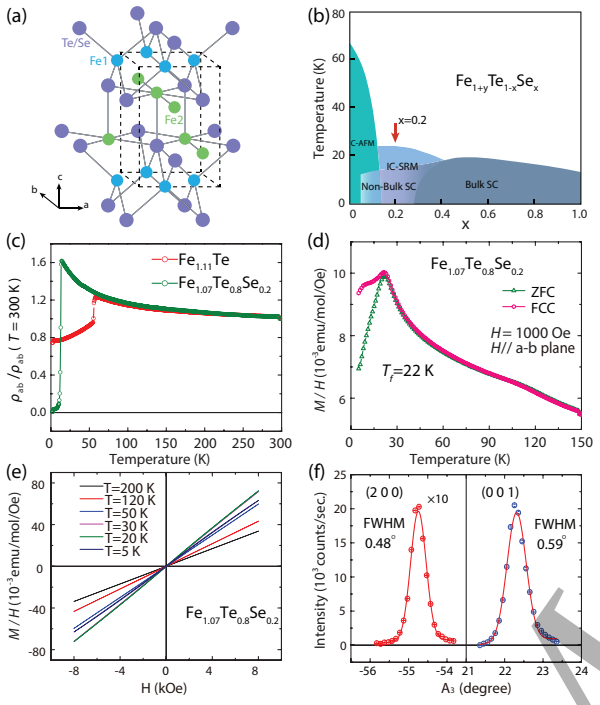

Figure 1: (a) Crystal structure of $Fe_{1+y}Te_{1-x}Se_x$ with Fe1 and the interstitial iron Fe2 marked as cyan and green balls, respectively. (b) Schematic phase diagram for $Fe_{1+y}Te_{1-x}Se_x$, where C, IC, SC, AFM and SRM denote commensurate, incommensurate, superconductivity, antiferromagnetic order and short-range magnetic order, respectively. (c) Temperature dependence of resistivity for $Fe_{1.07}Te_{0.8}Se_{0.2}$ and $Fe_{1.11}Te$. A filamentary SC is observed in $Fe_{1.07}Te_{0.8}Se_{0.2}$ and a simultaneous AFM and structural transition are seen in $Fe_{1.11}Te$. (d) Temperature dependence of DC magnetic susceptibility (χ(T) = M(T)/H) curves for $Fe_{1.07}Te_{0.8}Se_{0.2}$ at external in-plane magnetic field 1000 Oe. (e) M(H) measurements at several temperatures, which show that the excess iron is not ferromagnetic impurity but part of this crystal in $Fe_{1.07}Te_{0.8}Se_{0.2}$. (f) Nuclear Bragg peaks measured by neutron diffraction at 300 K for $Fe_{1.07}Te_{0.8}Se_{0.2}$.

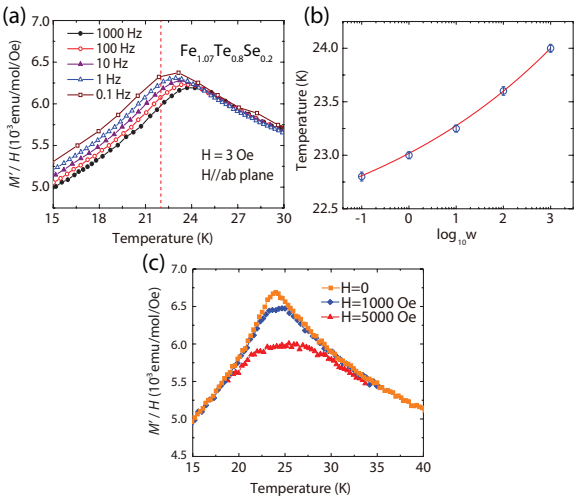

Figure 2: AC magnetic susceptibility of the $Fe_{1.07}Te_{0.8}Se_{0.2}$ sample. (a) Temperature dependence of AC magnetic susceptibility (χ'(T) = M'(T)/H) under a zero DC field and 3 Oe AC driving field at a series frequencies. The cusps shift systematically. (b) Frequency dependence of the freezing temperature T_f. The solid line denotes the best fitting to expression Eq.(1). (c) Temperature dependence of χ'(T) under an AC frequency of 1000 Hz in different DC fields.

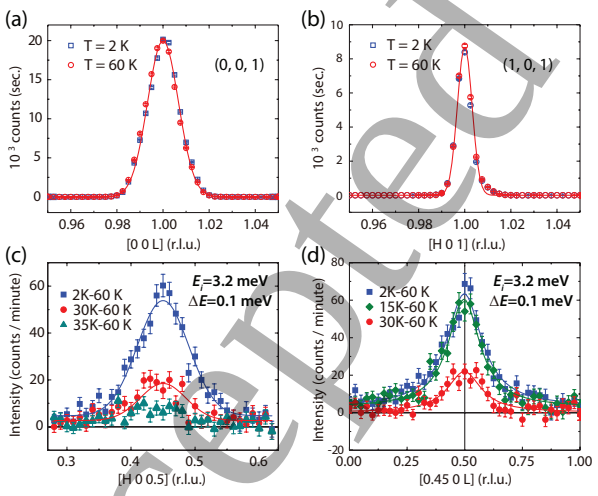

Figure 3: (a) and (b): Elastic longitudinal scans at the nuclear peaks (0,0,1) and (1,0,1) for $Fe_{1.07}Te_{0.8}Se_{0.2}$ measured at 2 K and 60 K. The lines are fit to a Gaussian function. (c) and (d): Temperature dependence of the longitudinal scans along the [H, 0, 0.5] and [0.45, 0, L] directions using the $T = 60$ K data as background scattering. The solid lines in the two figures are Gaussian and Lorentzian fits to the data respectively.

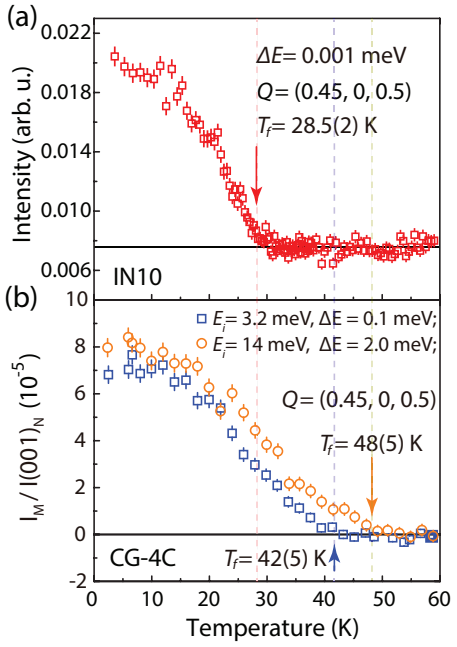

Figure 4: Instrumental energy-resolution dependence of spin glass freezing temperature. Magnetic order parameter measured with energy resolution (a) $\Delta E \sim 1$ μeV at neutron backscattering spectrometer IN10, ILL and (b) $\Delta E \sim 0.1$ meV and ~ 2 meV at CG-4C spectrometer, HFIR. The vertical dashed lines are used to guide the locations of T_f.

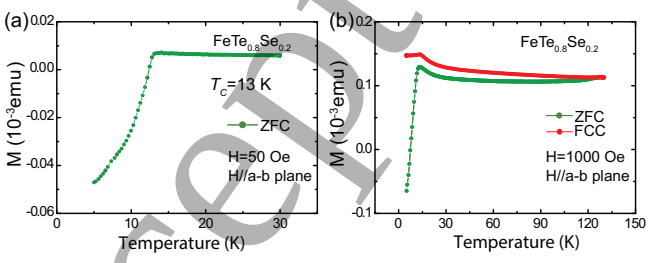

Figure 5: (a) ZFC magnetization measurements for annealed $FeTe_{0.8}Se_{0.2}$ with an in-plane magnetic filed 50 Oe. (b) ZFC and FCC magnetization measurements for annealed $FeTe_{0.8}Se_{0.2}$ with an in-plane magnetic filed 1000 Oe.